Journal of Physics D:
Applied Physics

PAPER • **OPEN ACCESS**

Simulation of metal nanoparticles growth in methane atmosphere of arc discharge: comparison to experiment

To cite this article: V Nemchinsky *et al* 2025 *J. Phys. D: Appl. Phys.* **58** 085207

OPEN ACCESS
IOP Publishing
Journal of Physics D: Applied Physics
J. Phys. D: Appl. Phys. **58** (2025) 085207 (11pp)
https://doi.org/10.1088/1361-6463/ad9ebd

Simulation of metal nanoparticles growth in methane atmosphere of arc discharge: comparison to experiment

V Nemchinsky, S Musikhin and Y Raitses*

Princeton Plasma Physics Laboratory, Princeton, NJ 08540, United States of America

E-mail: yraitses@pppl.gov

Received 1 September 2024, revised 20 November 2024
Accepted for publication 12 December 2024
Published 24 December 2024

Abstract

A direct current arc discharge in a methane atmosphere is a scalable and sustainable method to produce metal-carbon core–shell nanoparticles and single-walled carbon nanotubes, where a metal catalyst can be continuously supplied through evaporation of an anode made from the catalyst material. The size of catalyst particles is of critical importance as it can affect the synthesis yield and properties of nanotubes and core–shell nanoparticles. This study presents a numerical model describing the formation and growth of metal particles for the conditions representative of the arc discharge with an evaporating iron anode at near-atmospheric pressure of a methane-rich atmosphere. The model incorporates carbon adsorption to the metal surface and explains the limiting effect of carbon coverage on the size of metal nanoparticles. The predicted particle sizes are compared with experimental observations. The model also predicts higher concentrations of metal particles with the increasing partial pressure of methane.

Keywords: arc discharge, methane, core–shell nanoparticles, single-walled carbon nanotubes, numerical modeling

1. Introduction

Going back to the pioneering work by Iijima in 1991 [1], direct current (DC) anodic arc discharge remains one of the main methods for large-scale production of single-walled carbon nanotubes (SWCNTs) [2–6]. In its common implementation, the discharge is maintained between two graphite electrodes at near-atmospheric pressure of He and/or H_2. The anode ablation driven by arc heating provides a feedstock of carbon atoms and molecules for the synthesis of carbon nanotubes (CNTs). To sustain the growth of SWCNTs, metal catalyst, e.g. Fe, Co, Ni, Y, or their mixture [2–4], is typically added to the anode as a powder of microparticles, which evaporates in the hot arc environment and then nucleates and grows as nanoparticles. An alternative approach to ablating graphite anode is to supply carbon feedstock by pyrolytic decomposition of a hydrocarbon gas (e.g. CH_4) in the arc, while a metal catalyst (e.g. iron) can be supplied through evaporation of the anode made from this material. The use of methane, the greenhouse gas, as a precursor makes the approach sustainable and scalable, which was patented for commercial production of hydrogen and carbon black [7], as well as CNTs [8].

While methane arc has been successfully implemented for large-scale production of carbon black [7, 9] and metal-carbon core–shell particles [10–13], its use for high-yield synthesis of CNTs is yet to be optimized [14]. Among various optimization parameters, the size of metal catalyst particles was shown to affect, for example, the selectivity of CNTs synthesis and the number of nanotube walls. Chemical vapor deposition experiments at controlled conditions showed that

* Author to whom any correspondence should be addressed.

SWCNTs typically grow on catalyst particles under 3–5 nm, while larger catalyst particles lead to the formation of either multi-walled carbon nanotubes or core–shell particles [15–18]. In our previous work [14], we experimentally demonstrated that the growth of iron nanoparticles in methane arc discharge is intrinsically limited because of the developing carbon shell on the particle surface, which, if controlled, can be beneficial for the synthesis of CNTs. The effect of carbon coverage was explained through a simplified aerosol growth model using phenomenological terms. Essentially, a partially carbon-covered iron particle has a limited surface that is available to iron atoms condensation, which reduces the likelihood of iron atoms adsorption, and thus, slows down the particle growth. Similarly, a limited exposed iron surface reduces the chance of iron particles coalescing with each other. Overall, the carbon coverage effect was found to determine the metal particle size. However, no numerical model was presented that can accurately predict the size of metal particles produced in a hydrocarbon arc environment.

The growth of metal nanoparticles was modeled before in various contexts, including inert gas condensation, spark discharge, metal film laser ablation, sputtering, and welding arc [19–23]. Typically, the reported models considered particle nucleation based on the classical nucleation theory [24] and particle growth by condensation and collisions. In this paper, however, we address the growth of metal nanoparticles in the presence of hydrocarbons—a scenario relevant, but not limited, to CNTs synthesis in a hydrocarbon arc discharge.

We present a self-consistent numerical model that describes the formation and growth of iron clusters in a chemically active methane environment. Although the model development was motivated by the challenge of CNTs synthesis optimization, we do not consider the processes of tube nucleation and tube growth. Instead, the model focuses on the metal catalyst growth in a hydrocarbon environment, which is a prerequisite for CNTs formation in the methane arc discharge. We believe that the presented model could guide further experiments and give insights into how to control catalyst particle size and concentration without the need for comprehensive parametric studies. The paper is organized as follows. Section 2 describes the model: Governing equations, assumptions, and simulation parameters. Section 3 presents the modeling results in terms of metal particle size, concentration, and particle carbon coverage. The results are then compared with the experimental data [14].

2. Model description

The developed model intends to describe multiple processes, which are schematically shown in figure 1: Evaporation of iron atoms from a hot molten steel surface (different colors denote different temperature regions); Subsequent iron vapor diffusion into the cold buffer gas (e.g. argon), iron vapor cooling, and nucleation of clusters; Clusters growth by iron atoms condensation and clusters coalescence; Decomposition

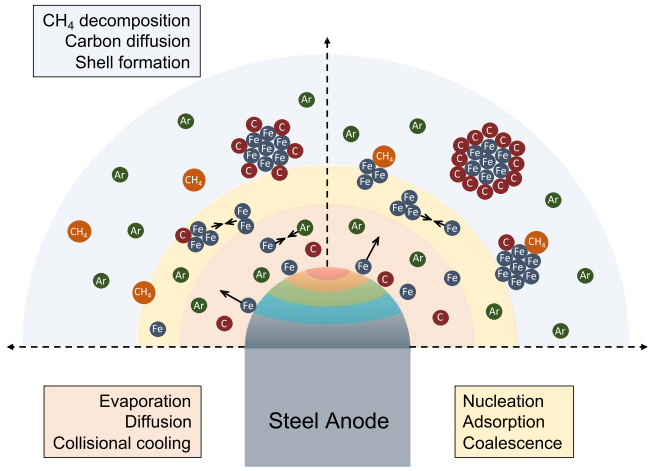

Figure 1. Schematics of the processes described by the model. Not up to scale. Colored areas on the anode surface represent different temperatures. Reproduced from [14]. © The Author(s). Published by IOP Publishing Ltd. CC BY 4.0.

of methane at the cluster surface; Carbon surface adsorption and carbon shell formation.

Several simplifications were adopted. First, it was assumed that iron vapor diffuses from the evaporating surface and expands symmetrically in space. Both iron atoms and clusters were characterized by a single diffusion coefficient, D, and a single temperature, T. The latter is different from the evaporating surface temperature, T_s. Ambient gas temperature was assumed to be constant, and the cluster size distribution monodisperse. The gas temperature inside the core of a similar DC arc was estimated to be between 0.5–1 eV, i.e. 5,000–12,000 K [25]. Hence, CH_4 molecules inside the arc are decomposed into their constituents, C and H atoms, which could recombine in different configurations (C_2, C_3, C_xH_y, etc.) when diffusing out of the arc. Here, we only account for a single decomposition product, the monoatomic carbon, and for methane that the reactor chamber is filled with. Finally, the model does not account for the charging of synthesized particles. For arc discharge systems, this assumption is based on several studies [26–28], which showed that the particle synthesis takes place away from a highly ionized hot arc core, in a colder periphery region where the degree of ionization is low.

2.1. Nucleation rate and cluster growth

Metal clusters formation by evaporation of the bulk metal into a buffer gas was investigated experimentally and numerically elsewhere [29–33]. In simulation studies, a classical nucleation theory and its modifications were often employed [24, 34, 35]. Here, we build our model based on a simplified, yet accurate, monodisperse approach described in [36]. However, unlike previous studies that focused on modeling metal condensation in an inert gas atmosphere, we consider a chemically active hydrocarbon gas. Under such conditions, along with metal atoms, methane or its decomposition products can adhere to and decompose on the metal cluster surface.

In the described model, the system of atoms and clusters evolves in time without considering spatial variations. Once the time dependences of all the parameters of interest are determined, one can indicate the corresponding particle location for any specific time. Namely, it was assumed that within a given time interval t, the particles would diffuse due to the density gradient by the distance $z = 2(Dt)^{1/2}$. We disregarded thermal diffusion because, as it will be shown later, the temperature variation is negligible compared to the density variation.

Clusters are born in the process of nucleation. A commonly accepted nucleation model developed by Girshick and Chiu [24], gives the nucleation rate (m^{-3} s^{-1})

$$J = \upsilon_1 \left(\frac{2\sigma}{\pi m_a}\right)^{1/2} N_a N_s \exp\left[\Theta - \frac{4\Theta^3}{27(\ln S)^2}\right], \qquad (1)$$

where σ is the metal surface tension (1.8 N m^{-1} here for iron [37]), N_a is the density of evaporated metal atoms, $N_s = N_s(T)$, is the saturated metal vapor density at a temperature, T [38], $S = N_a/N_s$, is the supersaturation value, while m_a and υ_1 are the monomer (iron atom) mass and volume, respectively. In equation (1), the parameter Θ is the dimensionless surface tension,

$$\Theta = \frac{\sigma s_1}{kT}, \qquad (2)$$

where k is the Boltzmann constant and s_1 is the monomer surface area. The monomer parameters are: $m_a = 9.27 \times 10^{-26}$ kg, $r_{Fe} = 156$ pm [39], $s_1 = 4\pi {r_{Fe}}^2$, and $\upsilon_1 = 4/3\pi {r_{Fe}}^3$. Clusters are born at a critical size of

$$g_c = \left(\frac{2\Theta}{3\ln(S)}\right)^3. \qquad (3)$$

The referred nucleation model [24] assumes an isothermal case when the nucleation heat is removed from the system. This approach is only suitable when a small fraction of clusters exists in the surrounding gas. However, the energy released during the nucleation can substantially heat the forming clusters (non-isothermal case). This nucleation heat shifts the system towards the lower supersaturation level thereby decreasing the nucleation rate. We included the correction for non-isothermal nucleation described in [40, 41]. Namely, using the terminology of [41], the nucleation rate reduction is accounted for by the factor, f_{sup}:

$$f_{sup} = \frac{J_{noniso}}{J_{iso}} = \frac{b^2}{b^2 + H^2}, \qquad (4)$$

where J_{iso} and J_{noniso} are the nucleation rates with and without thermal effects taken into account, $H = 3.62$ eV is the latent heat of iron evaporation [42], and

$$b^2 = 2k^2T^2\left(1 + \frac{N_{Ar}}{N_a}\sqrt{\frac{m_a}{m_{Ar}}}\right) \qquad (5)$$

describes the energy transfer between a monatomic cluster and monatomic carrier gas between two subsequent condensation/evaporation events. $N_{Ar} = P_{Ar}/kT_{gas}$, is the density of the buffer gas (argon here), $m_{Ar} = 6.63 \times 10^{-26}$ kg is the atomic mass of argon. To account for non-isothermal nucleation, the expression for nucleation rate (equation 1) is multiplied by f_{sup} (equation 4).

Our model considers iron atoms (density N_a) and clusters. Clusters are characterized by their number density N_g and size g, where $g = N_\upsilon/(N_g\upsilon_1)$ is the number of atoms in a cluster. $N_\upsilon = N_g\upsilon_g$ is the clusters volume density and υ_g is the volume of the cluster consisting of g atoms. The model consists of three rate equations: change of cluster volume density, change of the clusters number density, and the continuity equation. We follow the notation from [36]. But additionally account for the continuous coverage of clusters with carbon atoms.

The rate change of N_υ is given by

$$\frac{\partial N_\upsilon}{\partial t} = J\upsilon_1 g_c + \upsilon_1(1-\theta)\beta_{1-g}(N_a - N_s)N_g. \qquad (6)$$

The benefit of introducing N_υ is that it does not change during coalescence. In this equation, the first term describes cluster nucleation, while the second term describes the condensation of metal atoms on the cluster ($N_a > N_s$) or their evaporation from the cluster ($N_a < N_s$). Parameter β_{1-g} (m^3 s^{-1}) represents the frequency of collisions between iron monomers (atoms) and clusters consisting of g atoms. Details on the collision frequency are given in appendix A. θ is the fraction of the cluster surface occupied by the adsorbed carbon atoms. In the present model, we assume that once an adsorption site on the nanoparticle surface is occupied by a carbon atom, it is not available for metal atoms to condense. Hence, a partially carbon-covered iron particle has $1-\theta$ part of the surface that is available to iron atoms condensation. The carbon coverage process reduces the likelihood of iron atoms adsorption, and thus, slows down the iron particle growth. When fully encapsulated in carbon ($1-\theta = 0$), particle growth by condensation ceases. We assumed the degree of coverage to be the same for all clusters at a given time.

The clusters number density rate is given by

$$\frac{\partial N_g}{\partial t} = J - \frac{1}{2}(1-\theta)^2\beta_{g-g}N_g^2, \qquad (7)$$

where parameter $1/2$ is introduced so that the collisions between the same clusters are not counted twice, and β_{g-g} (m^3/s) is the frequency of the collisions between clusters, detailed in appendix A. The probability of two clusters coalescing with each other, each having $1-\theta$ part of the exposed metal surface, is $(1-\theta)^2$. A fully formed carbon shell entirely stops the coalescence.

Finally, the last rate equation stems from a continuity equation:

$$\frac{\partial}{\partial t}(\upsilon_1 N_a + N_\upsilon) = 0. \qquad (8)$$

We used the following initial conditions at the evaporating surface: $N_a = N_s$, $N_g = 0$, $N_\upsilon = 0$. Iron saturation density $N_s(T)$ corresponding to the evaporating surface temperature was taken from the Vienna TU database [38].

2.2. Clusters temperature distribution

Near the evaporating surface (anode top surface in the arc), the vapor is assumed to be at the surface temperature. As the vapor and newborn clusters diffuse away from this surface, they cool down through the collisions with the buffer gas and heat up through the condensation of iron atoms and the adsorption of carbon atoms. In our simplified model, we describe atoms and clusters as having a single temperature. Therefore, the cluster temperature variation is defined as

$$\frac{\mathrm{d}T}{\mathrm{d}t} = \frac{Q_1 + Q_2 + Q_3}{C_1 + C_2}, \tag{9}$$

where Q_1 is the energy exchange due to collisions between the buffer gas and metal atoms and clusters, Q_2 due to iron atoms condensation and evaporation, Q_3 due to carbon atoms adsorption to clusters, C_1 is the heat capacity of the iron vapor, and C_2 is the heat capacity of the clusters.

The heat exchange due to collisions with the buffer gas, Q_1 ($\mathrm{Wm^{-3}}$), is given by:

$$Q_1 = -2k\alpha\,(T - T_{\mathrm{gas}}) \sum_{\mathrm{i=Fe,\,g}} \left(\sqrt{\frac{8kT}{\pi\, m_{\mathrm{Ar}}}} S_{\mathrm{Ar-i}} N_{\mathrm{Ar}} N_{\mathrm{i}} \right), \tag{10}$$

where 'Fe' refers to an iron atom, 'Ar' to an argon atom, 'g' to a g-cluster, and $S_{\mathrm{Ar-i}} = \pi\,(r_{\mathrm{Ar}} + r_i)^2$ is the corresponding collision cross-section, e.g. $S_{\mathrm{Ar\text{-}Fe}} = \pi(r_{\mathrm{Ar}} + r_{\mathrm{Fe}})^2 = 1.6 \times 10^{-19}\ \mathrm{m^2}$, where $r_{\mathrm{Ar}} = 71$ pm, $r_{\mathrm{Fe}} = 156$ pm are the corresponding atomic radii [39]. In addition, we assumed that $S_{\mathrm{Ar-g}} = S_{\mathrm{Fe-Ar}} \times \mathrm{g}^{2/3}$. Here, since g represents the volume of an iron cluster, its surface is proportional to $g^{2/3}$. Parameter α is the thermal accommodation coefficient, which quantifies the efficiency of energy transfer during collisions between gas molecules and the surface of iron atoms or clusters. Its value is bound between 0, i.e. no energy exchange, and 1, i.e. complete thermalization of the gas atom to the cluster temperature upon the collision. Here, we assume α to be independent of cluster temperature and cluster size [43], although the opposite evidence exists in the literature [44, 45]. For the argon–iron pair, we adopt a constant value of $\alpha = 0.1$, which is an average derived from multiple experimental and molecular dynamics studies [45–48].

Technically, iron atoms and clusters also collide and exchange energy with methane molecules. Such interactions should be accounted for, similar to that of collisions with argon atoms. However, given the low concentration of methane in the gas mixture (Ar 97.6 wt.%, CH_4 2.4 wt.%), we neglected the impact of these collisions.

Clusters heat up due to iron atoms condensation ($N_{\mathrm{a}} > N_{\mathrm{s}}$) and cool down due to atoms evaporating from the cluster ($N_{\mathrm{a}} < N_{\mathrm{s}}$). The process depends on the exposed metal surface area, collision frequency between iron atoms and clusters, and clusters number density. Therefore, Q_2 ($\mathrm{Wm^{-3}}$), is given by

$$Q_2 = (1 - \theta)\,\beta_{1-\mathrm{g}}\,(N_{\mathrm{a}} - N_{\mathrm{s}})\,N_{\mathrm{g}} H. \tag{11}$$

The heat exchange due to the adsorption of carbon atoms, Q_3 ($\mathrm{Wm^{-3}}$), depends on concentrations and collision frequencies of methane and carbon atoms with clusters, their sticking coefficients, and the degree of cluster carbon coverage:

$$\begin{aligned} Q_3 = {} & \beta_{\mathrm{CH4-g}} N_{\mathrm{CH4}} N_{\mathrm{g}}\,[K_1\,(1 - \theta)]\,H_{\mathrm{ads}} \\ & + \beta_{\mathrm{C-g}} N_{\mathrm{C}} N_{\mathrm{g}}\,[K_2\,(1 - \theta)]\,H_{\mathrm{ads}}, \end{aligned} \tag{12}$$

where N_{CH4} is the density of methane molecules in the buffer gas, $N_{\mathrm{CH4}} = P_{\mathrm{CH4}}/kT_{\mathrm{gas}}$, N_{C} is the density of carbon atoms (originating from the hot arc), K_1 represents the probability of methane decomposition at the iron cluster surface, and K_2 is the probability of C atoms to adsorb to the cluster surface, i.e. 'sticking coefficient'. Adsorption of carbon atoms brings the adsorption heat, $H_{\mathrm{ads}} = 6$ eV [49, 50] to the iron cluster. Methane decomposition over carbon surfaces is typically low unless the surface is activated [51]. Therefore, we consider methane decomposition only at the metal part of the cluster surface. Note that after the metal cluster is encapsulated by a single-layer carbon shell, the shell continues to grow in thickness, which is evident from numerous TEM images [10–14]. However, that process was not of interest in this study.

The probability of CH_4 decomposition at the iron cluster surface, K_1, is given by

$$K_1 = K_0 \exp\left(-\frac{H_{\mathrm{ma}}}{kT}\right), \tag{13}$$

where $K_0 = 0.05$ is the pre-exponential factor and $H_{\mathrm{ma}} = 0.575$ eV is the energy of methane activation. In the absence of data for iron, values were obtained from experimental sticking coefficients for CH_4 on nickel [52]. Data for Ni (100) and (110) crystal planes were averaged and extrapolated from the available temperature range of 450–600 K to temperatures relevant for this study, i.e. 800–2500 K. The plane selection was informed by literature, suggesting that the activation energies for methane on nickel and iron are the highest on the (100) and (110) surfaces [53–55].

The sticking coefficient for carbon atoms adsorbing to the iron surface, K_2, is not known. Based on the limited data for several other atoms impingent on metal surfaces, including nickel surfaces, we assume a temperature-independent $K_2 = 0.3$ [56]. We comment on the impact of the uncertainty of this parameter on the calculated particle size in section 3 of the paper.

The volumetric heat capacity of the iron vapor, C_1 ($\mathrm{J\,K^{-1}\,m^{-3}}$), is defined as

$$C_1 = \frac{3}{2} k N_{\mathrm{a}}, \tag{14}$$

and the volumetric heat capacity of clusters, C_2, as

$$C_2 = C\rho N_{\upsilon} = C\rho \upsilon_1 g N_{\mathrm{g}}, \tag{15}$$

where $\rho = 7800\ \mathrm{kg/m_3}$ and $C = 450\ \mathrm{J/kg/K}$ are the iron density and heat capacity [57], and $\upsilon_1 g$ is the g-cluster volume.

2.3. Degree of coverage

The degree of cluster surface covered by the adsorbed carbon atoms is determined by the competition of three processes: carbon atoms adsorption, evaporation of already adsorbed carbon atoms, and diffusion of carbon atoms from the surface into the bulk of the cluster. Let $G_{\rm ads}$, $G_{\rm evap}$, and $G_{\rm diff}$ be the densities of the corresponding fluxes, respectively. Also, let a_L be the distance between adsorbed carbon neighbors so that $1/a_L^2$ is the surface density of the sites available for carbon atoms adsorption. Then, the time dependence of the degree of coverage can be found as

$$\frac{{\rm d}\theta}{{\rm d}t} = a_L^2\left(G_{\rm ads} - G_{\rm evapor} - G_{\rm diff}\right) - \theta\frac{2}{R}\frac{{\rm d}R}{{\rm d}t}, \qquad (16)$$

where the last term accounts for the change of the carbon surface density due to the iron cluster growth (increase in radius R) while the number of carbon atoms on the surface is constant. The derivation is given in appendix B. Calculations showed that this term is only substantial at the very early stages of the cluster development and thus, was neglected here. The distance a_L can be estimated as $(m_{\rm a}/\rho)^{1/3}$, which gives $a_L \sim 2.2$ Å.

The deposition of carbon on the metal nanoparticle, $G_{\rm ads}$, is described by thermal fluxes of methane molecules and carbon atoms to the nanoparticle surface,

$$G_{\rm ads} = K_1\left(1-\theta\right)\frac{1}{4}N_{\rm CH4}\bar{\upsilon}_{\rm CH4} + K_2\left(1-\theta\right)\frac{1}{4}N_{\rm C}\bar{\upsilon}_{\rm C}, \qquad (17)$$

where $\bar{\upsilon}_{\rm CH4}$ and $\bar{\upsilon}_{\rm C}$ are the methane and carbon atom thermal velocities. The evaporation of the adsorbed carbon atoms from the nanoparticle can be described as

$$a_L^2 G_{\rm evapor} = \theta\omega\exp\left(-H_{\rm ads}/kT\right), \qquad (18)$$

where ω is the oscillation frequency of an adsorbed carbon atom [58]. One can see that even if assuming $\omega = H_{\rm ads}/h$, where h is the Planck constant, i.e. when grossly overestimating the oscillation frequency, and assuming the highest temperature investigated here (~2600 K, explained in section 2.4), the thermal desorption is still negligible. Finally, the diffusion of adsorbed carbon atoms from the surface into the bulk of the iron cluster is considered in appendix C. It is shown that even for the cluster temperature of 2600 K, clusters become fully encapsulated before any significant number of carbon atoms diffuse into the cluster bulk. Thus, the $G_{\rm diff}$ term was also neglected.

2.4. Parameters of simulation

Although the model is not tied up to a specific experiment, we used some of the experimental parameters from [14] and [59], which allowed us to validate the model against these experimental data. Experiments were conducted for the arc discharge between the anode made from low-carbon steel (ASTM A36) and the cathode made from 2% ceriated tungsten. Two different gas atmospheres were used: 100% Ar (67 kPa) and Ar (67 kPa) + 2.4 wt.% CH_4 (1.6 kPa). In both these cases, the same arc current of 30 A was used. The synthesized particles were analyzed and measured using transmission electron microscopy (TEM) and energy dispersive x-ray spectroscopy. Measurements of the gas temperature using a thermocouple placed at the arc periphery yielded $T_{\rm gas} = 800$ K, which suggests minimal methane pyrolysis [60]. Here, we assumed no methane pyrolysis outside of the arc. However, the gas temperature inside a similar DC arc was estimated to be 5,000–12,000 K [25], hence, methane should decompose inside the arc. Considering the isobaric conditions inside and outside of the arc, and given the gas mixture composition (67 kPa Ar + 1.6 kPa CH_4) and the gas temperature outside of the arc (800 K), we estimated that the concentration of C atoms leaving the arc should amount to ~1%–2% of the CH_4 concentration outside of the arc. Once leaving the arc, carbon atoms expand in space, adsorb to iron clusters, adsorb to other carbon atoms to form soot particles, and recombine with hydrogen and other radicals to form C_xH_y species. The latter two processes were not simulated here. Temperature fields of the evaporating anode surface were obtained using thermal imaging [59]. The radii, $r_{\rm i}$, of isotherms with corresponding temperatures $T_{\rm i}$ are given in table 1.

Table 1. Experimental isotherms of the evaporating steel anode at typical arc discharge conditions [59].

Argon		Argon + 2.4 wt. % Methane	
$T_{\rm i}$ (K)	$r_{\rm i}$ (mm)	$T_{\rm i}$ (K)	$r_{\rm i}$ (mm)
2500	0.1	2200	0.1
2450	0.25	2150	0.55
2350	0.8	2050	1.1
2250	1.35	1950	1.6
2150	1.6	1850	2.9
2050	2.1		
1950	2.65		

To keep the model 1D instead of converting it to 2D, we approximate experimental temperature fields as a single circular area having a uniform temperature and assume a symmetrical vapor expansion from the obtained area. First, we calculate the total iron evaporation rate, Γ (kg s^{-1}), using the Hertz–Knudsen equation,

$$\Gamma = \sum_{\rm i}\left(A_{\rm i}P_{\rm i}\sqrt{\frac{m_a}{2\pi kT_{\rm i}}}\right) \qquad (19)$$

where $A_{\rm i}$ is the area of the corresponding isotherm (circle for the first isotherm and outer circular rings for the rest, see colored areas in figure 1), $P_{\rm i}$ is the equilibrium iron vapor pressure at $T_{\rm i}$, and $m_{\rm a}$ is the mass of an iron atom. Next, we define circular areas within which 50 and 90% of the total evaporation, Γ, occurs. For the case of pure argon, this yields $R_{\rm Ar,50\%} = 0.85$ mm, and $R_{\rm Ar,90\%} = 1.8$ mm. Finally, we select a single temperature for each of the obtained areas so that the modeled evaporation rate matches the total experimental evaporation rate, Γ. This results in $T_{\rm Ar,50\%} = 2600$ K and $T_{\rm Ar,90\%} = 2400$ K. A similar analysis for the Ar/CH_4 mixture provides $R_{\rm Ar/CH4,50\%} = 1.2$ mm, $T_{\rm Ar/CH4,50\%} = 2260$ K, and $R_{\rm Ar/CH4,90\%} = 2.4$ mm, $T_{\rm Ar/CH4,90\%} = 2080$ K.

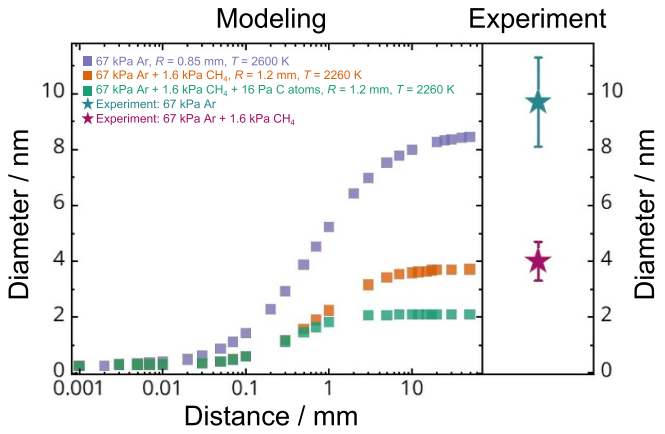

Figure 2. Metal core size versus distance from the evaporating source for pure Ar and Ar/CH_4 mixture with and without contribution from carbon atoms produced in the arc core considered. Asterisks denote the experimental measurements from [14]; squares show modeling results. Evaporating surface radii and temperatures were chosen based on the experimental evaporation rates.

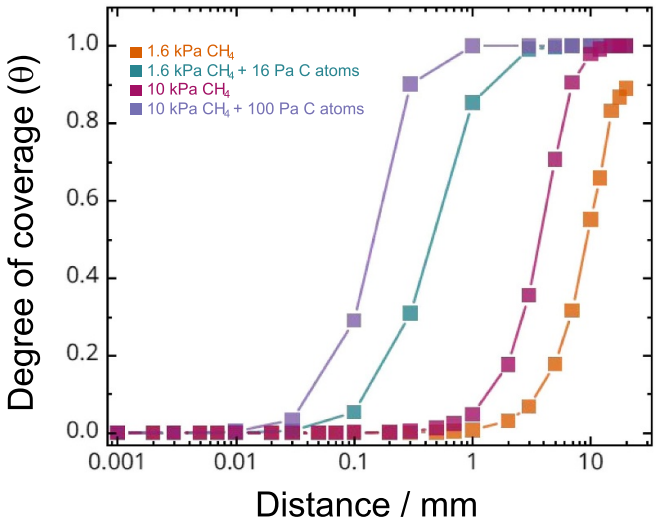

Figure 3. The degree of iron cluster coverage with carbon atoms, θ, versus distance from the evaporating source for different CH_4 and C atoms partial pressures. In all cases, argon pressure was 67 kPa. Evaporation spot set as $R_{Ar/CH4,50\%} = 1.2$ mm and evaporation temperature $T_{Ar/CH4,50\%} = 2260$ K. Lines are guides for the eye.

3. Results

Figure 2 shows the size of iron nanoparticles versus the distance from the evaporating anode surface. The results of the model are shown with squares, while the asterisks denote experimental data from [14]. As measured using TEM. For the TEM analysis, the particles were sampled much further from the evaporation surface than modeled here, therefore, the results are shown in an adjacent graph with no specified distance. Simulations for the 50% and 90% evaporation areas yielded similar results. Therefore, for clarity, figure 2 only presents the results for the 50% evaporation area, while both cases are shown in figure A4. For the pure argon, there is a fair agreement between the model and experimental results. Specifically, the model predicts iron clusters to grow up to 8–9 nm, while experiments yielded metal nanoparticles in the range of 8–11 nm. With the addition of methane, the model predicts the iron particle growth to halt at ∼3–4 nm. At this point, the metal nanoparticle is fully encapsulated by carbon. Experimental measurements yielded a similar iron core size of 3–5 nm. When additionally including carbon atoms into consideration, $N_C = 0.01 \times N_{CH4}$, with the sticking coefficient $K_2 = 0.3$, the iron particle size decreases to 2.1 nm. Given the large uncertainty in the sticking coefficient, we also calculated the particle size with $K_2 = 1$, which further reduced the particle size to 1.3 nm. Notably, for iron particles growing in pure argon, a case that did not include any uncertain empirical parameters, the model showed good agreement with the experiment.

From a practical standpoint, e.g. for the optimization of SWCNTs synthesis, it is interesting to analyze how the size of metal nanoparticles depends on the methane partial pressure. Figures 3 and 4 show the effect of the methane pressure on the carbon coverage of the metal particles and their size, respectively. All curves were obtained for $R_{Ar/CH4,50\%} = 1.2$ mm, $T_{Ar/CH4,50\%} = 2260$ K. The model predicts that iron clusters develop a carbon shell at distances between 1–10 mm from the evaporating surface when considering only catalytic methane decomposition and excluding the contribution from carbon atoms originating from the arc core. As anticipated, the higher the partial pressure of methane, the more rapidly the carbon shell develops. When completed, the carbon shell prevents the adsorption of new iron atoms and the coalescence of iron clusters, hence ceasing iron core growth. Additional carbon atoms may continue to adhere to the carbon shell making it thicker and increasing the overall particle size, which was observed in the experiment [14]. The growth of iron particles is predicted to stop at a size of 3–4 nm. However, when also accounting for the adsorption of carbon atoms, iron particles are expected to become encapsulated within 1 mm from the evaporating surface (figure 3) and to grow to a size of 0.7–1.3 nm (figure 4). This represents a significant underestimation compared to the experimentally observed particle size of 3–5 nm. Despite the discrepancy between the model and experimental results, we acknowledge that methane should indeed decompose inside the arc [61], and hence, carbon atoms should be considered. However, the extent of this decomposition and the kinetics of the resultant products recombination cannot be accurately estimated without knowledge of the chemical composition of the arc, its plasma properties, and spatially resolved gas temperatures. Nevertheless, the fact that our simplified model shows good agreement with the experiment in the case of pure argon, and accurately predicts the size trends in a chemically active hydrocarbon environment, suggests that the main particle growth processes were correctly captured.

The carbon shell formed around iron clusters also affects the density of iron nanoparticles in the gas volume (figure 5). When diffusing away from the evaporating anode surface, the

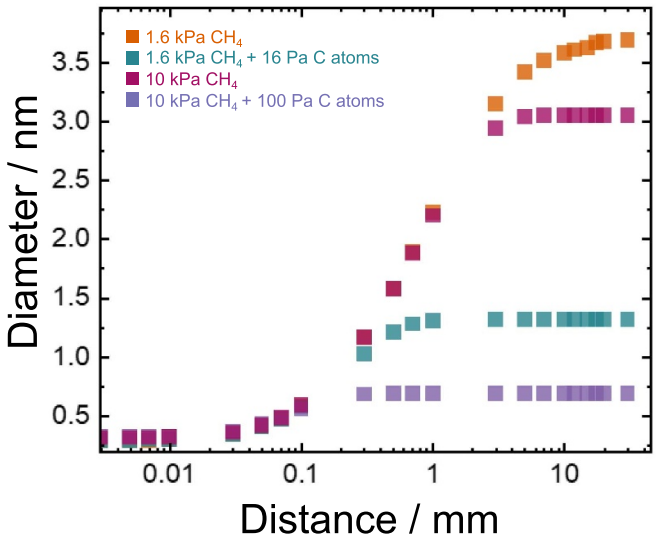

Figure 4. Metal core size versus distance from the evaporating source for Ar/CH_4 mixtures with different CH_4 and C atoms partial pressures. In all cases, argon pressure was 67 kPa. Evaporation spot set as $R_{Ar/CH4,50\%} = 1.2$ mm and evaporation temperature $T_{Ar/CH4,50\%} = 2260$ K.

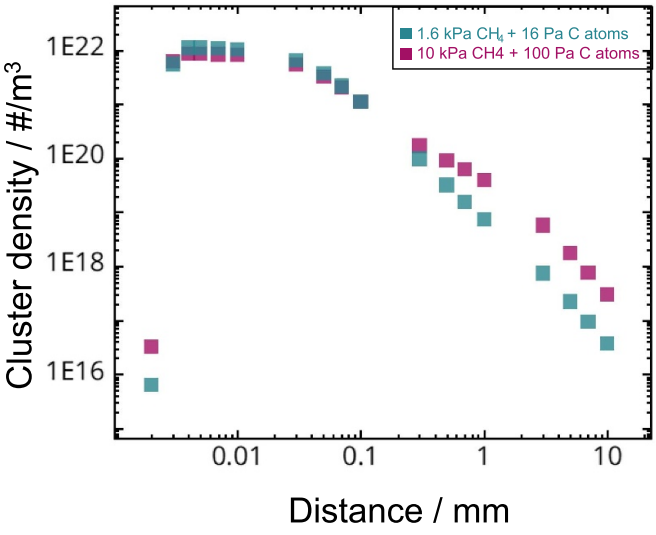

Figure 5. Iron clusters density versus distance from the evaporating source for Ar/CH_4 mixtures with different CH_4 and C atoms partial pressures. In all cases, argon pressure was 67 kPa. Evaporation spot set as $R_{Ar/CH4,50\%} = 1.2$ mm and evaporation temperature $T_{Ar/CH4,50\%} = 2260$ K.

gas temperature rapidly drops leading to high supersaturation, which prompts nucleation and a corresponding rise in the density of clusters (see appendix D for additional graphs). Counteracting to that, iron atoms are consumed by the formation of the iron clusters. Furthermore, the density of iron atoms decreases with vapor expansion in space leading to lower supersaturation values. From the moment the atom density drops below the saturation value, no new clusters are born. The existing clusters continue to coalesce and expand in space, therefore, their density decreases. However, the rate of the density decrease depends on methane partial pressure. At higher methane pressures, clusters are covered with carbon atoms faster, which lowers the likelihood of iron clusters coalescing with each other. Hence, with higher additions of methane, i.e. with faster carbon shell formation, iron clusters are consumed at a slower rate, as depicted in figure 5.

4. Conclusions

The DC arc discharge with an evaporating metal anode at near-atmospheric pressure of a methane-rich atmosphere is a scalable and sustainable method for the production of metal-carbon core–shell nanoparticles and SWCNTs. Here, a numerical model was developed to simulate the formation and growth of iron particles at conditions representative of that process. The model describes iron evaporation from the anode surface, clusters nucleation, and particle growth through condensation and coalescence. Additionally, the model incorporates carbon adsorption to the iron particle surface leading to the carbon shell formation, which was predicted to limit the metal core growth. For the conditions of the benchmark experiment, iron particles were predicted to become encapsulated by carbon at sizes between 2–4 nm in an Ar/CH_4 mixture, while in pure Ar particles were predicted to grow to 8–9 nm. Both results are in fair agreement with experimental observations. The model also predicted the increasing rates of carbon coverage and higher concentrations of metal particles with the increasing methane pressure. The developed model could guide future arc discharge experiments aiming to control catalyst particle size and optimize SWCNTs or core–shell nanoparticle production.

A more detailed modeling approach is justified when more comprehensive experimental data become available on chemical composition of the arc core and its plasma properties, as well as on particle properties, e.g. the temperature-dependent sticking coefficients for carbon atoms adsorbing to iron and carbon clusters. With such data, a more comprehensive model could incorporate different temperatures and diffusion coefficients for iron atoms and iron clusters, include spatially resolved gas temperatures, and be expanded to 2D simulations. The required gas temperatures could be measured using *in situ* spectroscopic techniques, while spatially resolved particle size measurements for model validation could be obtained with laser-induced incandescence.

Data availability statement

All data that support the findings of this study are included within the article (and any supplementary files).

Acknowledgment

This work was supported by the U.S. Department of Energy through contract DE-AC02-09CH11466. We thank Hengfei Gu and Bruce Koel (both from Princeton University) for fruitful discussions.

Appendix A. Collision frequency

In general, collision frequency between different particles depends on the relation between the mean free path of particles, λ, and their size [62, 63]. For particles much smaller than λ, the collision frequency between *i*-mere and *k*-mere species can be calculated as

$$\beta_{\mathrm{i-k}} = \left(\frac{3}{4\pi}\right)^{1/6}\left(\frac{6kT}{\rho}\right)^{1/2}\left(\frac{1}{v_{\mathrm{i}}}+\frac{1}{v_{\mathrm{k}}}\right)^{1/2}\left(v_{\mathrm{i}}^{1/3}+v_{\mathrm{k}}^{1/3}\right)^{2}, \tag{A1.1}$$

where k is the Boltzmann constant, v_{i} and v_{k} are volumes of the corresponding g-mers, and ρ is the density of iron. In the opposite case of particles larger than their mean free path, their collisions are a result of particles diffusion. The collision frequency then is

$$\beta_{\mathrm{i-k}} = \frac{2kT}{3\mu}\left(\frac{1}{v_{\mathrm{i}}^{1/3}}+\frac{1}{v_{\mathrm{k}}^{1/3}}\right)\left(v_{\mathrm{i}}^{1/3}+v_{\mathrm{k}}^{1/3}\right). \tag{A1.2}$$

where μ is the temperature-dependent dynamic viscosity of argon [64].

The frequency of atoms colliding with clusters, $\beta_{\mathrm{1-g}}$, depends on the regime, which can be kinetic or diffusion. The corresponding criterion is based on a comparison of the atom's mean free path λ and the distance between the atom and the nearest cluster [63]. Assuming the distance between the atom and the nearest cluster is ${N_{\mathrm{a}}}^{-1/3}$, we came up with the criterion ${N_{\mathrm{a}}}^{-1/3}(S_{\mathrm{a,gas}} \times N_{\mathrm{gas}})^{-1}$. For all the conditions investigated here, ${N_{\mathrm{a}}}^{-1/3}(S_{\mathrm{a,gas}} \times N_{\mathrm{gas}})^{-1} \gg 1$, which means that atoms reach the nearest cluster without collisions with buffer gas. Therefore, formula (A1.1) should be used for $\beta_{\mathrm{1-g}}$. Same applies to $\beta_{\mathrm{CH4-g}}$ and $\beta_{\mathrm{C-g}}$.

Appendix B. Carbon coverage

When the metal cluster's surface S is growing due to iron atoms adsorption and coalescence, but the number of carbon atoms on the surface is constant (N), the degree of coverage $\theta = \frac{N}{S}$ is decreasing. Following a few mathematical steps, we come to the final form of equation (16) in the main text.

$$\frac{1}{\theta}\frac{\mathrm{d}\theta}{\mathrm{d}t} = -\frac{1}{S}\frac{\mathrm{d}S}{\mathrm{d}t}$$

$$\frac{1}{s}\frac{\mathrm{d}S}{\mathrm{d}t} = \frac{2}{R}\frac{\mathrm{d}R}{\mathrm{d}t}.$$

Finally,

$$\frac{\mathrm{d}\theta}{\mathrm{d}t} = -\theta\frac{2}{R}\frac{\mathrm{d}R}{\mathrm{d}t}.$$

Appendix C. Carbon bulk diffusion

It can be shown that there is no substantial bulk diffusion in our case for two interrelated reasons:

1. Too slow diffusion. The characteristic time of nanoparticle cooling can be estimated as $t_{\mathrm{cool}} = R^2/a$, where R is the nanoparticle radius and $a \sim 10^{-5}\,\mathrm{m^2\ s^{-1}}$ is the iron thermal diffusivity [65]. For $R = 5$ nm, $t_{\mathrm{cool}} \sim 2 \times 10^{-12}$ s. During this time, the bulk diffusion front moves by distance $\delta \sim (D_{\mathrm{b}}t_{\mathrm{cool}})^{1/2}$, where D_{b} is the coefficient of carbon diffusion in iron. According to Tibbetts [66], $D_{\mathrm{b}}(2600\ \mathrm{K}) = 3 \times 10^{-8}\ \mathrm{m^2\ s^{-1}}$ and $D_{\mathrm{b}}(1000\ \mathrm{K}) = 5 \times 10^{-13}\,\mathrm{m^2\ s^{-1}}$. Correspondingly, at the highest temperature of $T = 2600$ K, $\delta \sim 3 \times 10^{-10}\,\mathrm{m} \ll R$. At lower temperatures, δ is even smaller.

2. Too fast encapsulation. Let us introduce a parameter Ω, equal to the ratio of carbon atoms flux arrival at the surface to the flux of their removal from the surface by diffusion. For the first flux, one has $F_{\mathrm{in}} = {}^1\!/_4 N_{\mathrm{CH4}}\bar{v}_{\mathrm{CH4}}$. N_{CH4} and $\bar{v}_{\mathrm{CH4}}$ are the density and thermal velocity of methane molecules, respectively. The flux of the adsorbed atoms inside the cluster can be estimated as $F_{\mathrm{out}} = D_{\mathrm{b}}n/R$, where n is the volume density equivalent to the adsorbed atoms surface coverage:$n = \frac{\gamma\theta}{a_L^3} = \frac{\gamma\theta}{V_{\mathrm{cell}}}$, where V_{cell} is the volume of the elementary cell of iron crystal calculated as the mass of the iron atom divided by the iron density and γ is the maximum solubility of carbon in iron. Correspondingly, we have an estimation:

$$\Omega = \frac{F_{\mathrm{in}}}{F_{\mathrm{out}}} = \frac{1}{4\gamma}N_{\mathrm{methane}}V_{\mathrm{cell}}\frac{\bar{v}_{\mathrm{CH4}}R}{D_{\mathrm{b}}}. \tag{A3.1}$$

This parameter strongly depends on temperature. At 2600 K and 1 kPa methane pressure, it is on the order of unity, but it increases very fast as temperature decreases so that at 1000 K, it is in the order of ∼1000. This means that the cluster becomes encapsulated before any substantial amount of carbon diffuses inside.

Appendix D. Additional graphs

Figure A1 shows the size of iron nanoparticles versus the distance from the anode surface for all simulated cases.

Figure A2 shows the supersaturation parameter and the iron nucleation rate versus distance from the evaporating surface. All points were obtained for the evaporation temperature $T_{\mathrm{Ar/CH4,50\%}} = 2260$ K and 1.6 kPa partial methane pressure with no contribution from carbon atoms considered. Supersaturation, $S = N_{\mathrm{a}}/N_{\mathrm{s}}(T) > 1$, occurs when there is a rapid drop in vapor temperature, so that the saturation density, $N_{\mathrm{s}}(T)$, becomes low, while the actual density of iron atoms, N_{a}, is still high. At the evaporating surface, the S value is close to unity and there is almost no nucleation. Away from the surface, as the gas temperature drops (here, to 800 K [59]), the supersaturation value increases, and the nucleation rate rapidly rises. Substantial nucleation takes place in a relatively narrow region, less than 0.01 mm away from the evaporating surface. The equilibrium condition, $S = 1$, is established at ∼0.4 mm

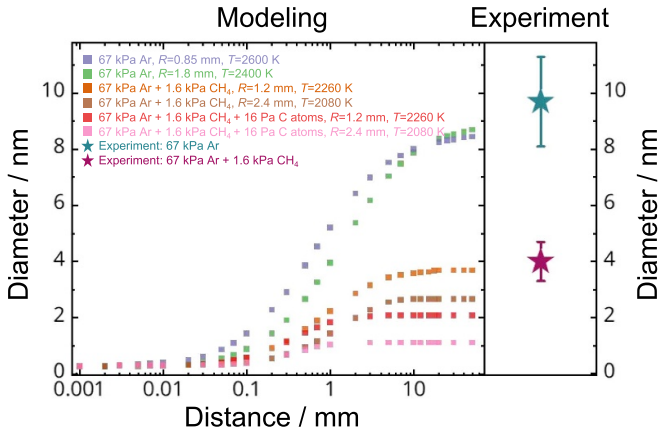

Figure A1. Metal core size versus distance from the evaporating source for pure Ar and Ar/CH_4 mixture. Asterisks denote the experimental measurements from [14].; squares show modeling results. Evaporating surface radii and temperatures were chosen based on the experimental evaporation rates.

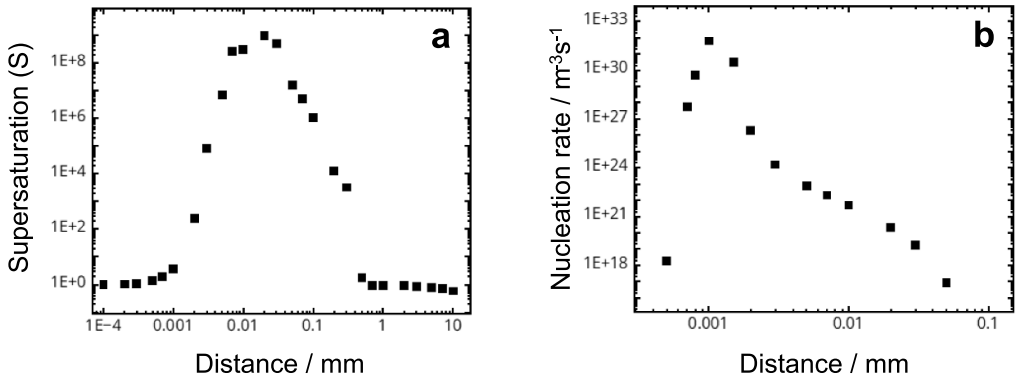

Figure A2. (a) Supersaturation level, S, and (b) Iron clusters nucleation rate versus distance from the evaporating surface. CH_4 partial pressure 1.6 kPa in 67 kPa of argon. Evaporation spot set as $R_{Ar/CH4,50\%} = 1.2$ mm and evaporation temperature $T_{Ar/CH4,50\%} = 2260$ K.

distance, beyond which, while the N_a decreases due to vapor expansion, the gas temperature and the corresponding $N_s(T)$ remain constant (note the model assumption $T_{gas} = \text{const}$). Hence, the S value falls lower than unity.

Iron clusters, once born, undergo condensation of iron atoms on their surface and coalescence with other iron clusters. The rates of these processes are shown in figure A3 for the $T_{Ar/CH4,50\%} = 2260$ K and 1.6 kPa partial methane pressure with no contribution from carbon atoms considered. It can be seen that condensation and coalescence are 'separated' in space. The intensity of condensation is proportional to the cluster density, N_g, and the level of supersaturation, S. Correspondingly, condensation begins almost immediately with the formation of clusters and intensifies as more clusters are born, but it decreases as the atom density falls. The coalescence rate, proportional to $N_g{}^2$, is initially slow while the cluster density is low, but rapidly increases during clusters formation. As clusters are consumed during coalescence, the rate is decreasing. Additionally, as clusters expand in space, N_g decreases, further slowing the coalescence rate.

Figure A4 shows atom and cluster densities versus distance from the evaporating surface. Initially, N_a reaches the saturation value of 1.6×10^{22} m^{-3} at 2260 K. Beyond 0.001 mm from the evaporating surface, N_a rapidly drops, i.e. no new iron atoms are supplied while the density of the existing atoms decreases due to adsorption. Cluster density, N_g, rises due to nucleation and declines due to coalescence.

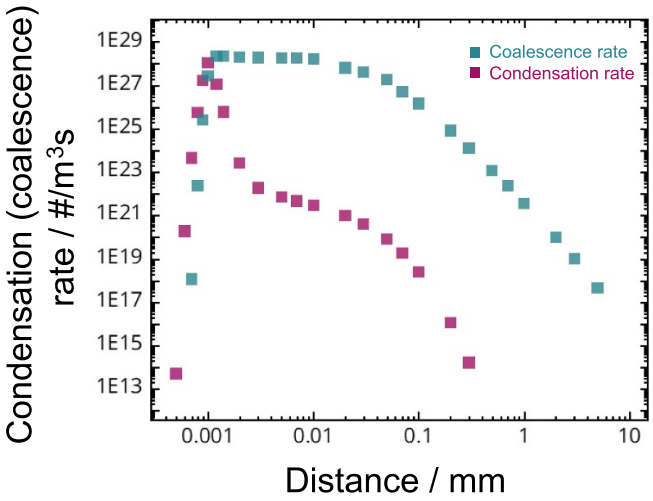

Figure A3. Condensation and coalescence rates vs. distance from the evaporating surface. CH_4 partial pressure 1.6 kPa in 67 kPa of argon. Evaporation spot set as $R_{Ar/CH4,50\%} = 1.2$ mm and evaporation temperature $T_{Ar/CH4,50\%} = 2260$ K.

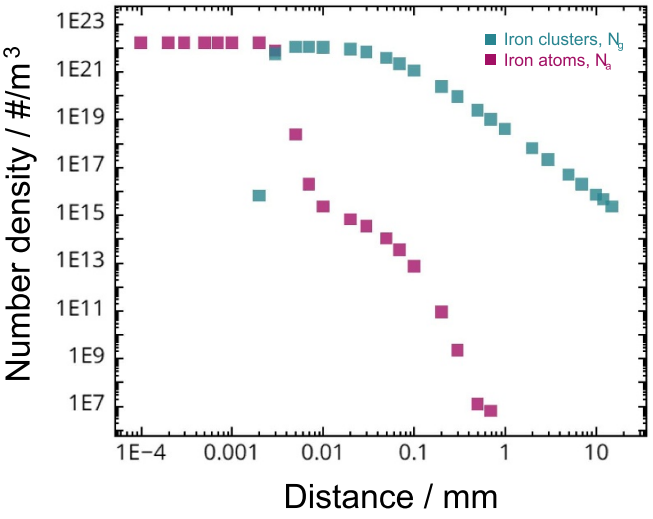

Figure A4. Densities of metal atoms (N_a) and clusters (N_g) versus distance from the evaporating surface. CH_4 partial pressure 1.6 kPa in 67 kPa of argon. Evaporation spot set as $R_{Ar/CH4,50\%} = 1.2$ mm and evaporation temperature $T_{Ar/CH4,50\%} = 2260$ K.

ORCID iDs

V Nemchinsky https://orcid.org/0000-0002-6064-7354
S Musikhin https://orcid.org/0000-0002-0199-6095
Y Raitses https://orcid.org/0000-0002-9382-9963

References

[1] Iijima S 1991 Helical microtubules of graphitic carbon *Nature* **354** 56–58
[2] Arora N and Sharma N N 2014 Arc discharge synthesis of carbon nanotubes: comprehensive review *Diam. Relat. Mater.* **50** 135–50
[3] Yatom S, Selinsky R S, Koel B E and Raitses Y 2017 Synthesis-on" and "synthesis-off" modes of carbon arc operation during synthesis of carbon nanotubes *Carbon* **125** 336–43
[4] Das R, Shahnavaz Z, Ali M E, Islam M M and Abd Hamid S B 2016 Can we optimize arc discharge and laser ablation for well-controlled carbon nanotube synthesis? *Nanoscale Res. Lett.* **11** 510
[5] Shi Z, Lian Y, Liao F H, Zhou X, Gu Z, Zhang Y, Iijima S, Li H, Yue K T and Zhang SL 2000 Large scale synthesis of single-wall carbon nanotubes by arc-discharge method *J. Phys. Chem. Solids* **61** 1031–6
[6] Keidar M, Shashurin A, Li J, Volotskova O, Kundrapu M and Zhuang T S 2011 Arc plasma synthesis of carbon nanostructures: where is the frontier? *J. Phys. D: Appl. Phys.* **44** 174006
[7] Johnson P L, Hanson R J, Carlos S and Taylor R W 2017Plasma Reactor. *US patent 9,574,086 B2*
[8] Predtechenskiy M R 2020 Method and apparatus for producing carbon nanostructures *US patent* US20200239316A1
[9] Gautier M, Rohani V and Fulcheri L 2017 Direct decarbonization of methane by thermal plasma for the production of hydrogen and high value-added carbon black *Int. J. Hydrogen Energy* **42** 28140–56
[10] Dong X L, Zhang Z D, Xiao Q F, Zhao X G, Chuang Y C, Jin S R, Sun W M, Li Z J, Zheng Z X and Dong X L 1998 Characterization of ultrafine -Fe(C), -Fe(C) and Fe_3C particles synthesized by arc-discharge in methane *J. Mater. Sci.* **33** 1915–9
[11] Hao C, Xiao F and Cui Z 2008 Preparation and structure of carbon encapsulated copper nanoparticles *J. Nanopart. Res.* **10** 47–51
[12] Zhang X, Rao Y, Guo J and Qin G 2016 Multiple-phase carbon-coated $FeSn_2$/Sn nanocomposites for high-frequency microwave absorption *Carbon* **96** 972–9
[13] Sunny V, Sakthi Kumar D, Yoshida Y, Makarewicz M, Tabiś W and Anantharaman M R 2010 Synthesis and properties of highly stable nickel/carbon core/shell nanostructures *Carbon* **48** 1643–51
[14] Musikhin S, Nemchinsky V and Raitses Y 2024 Growth of metal nanoparticles in hydrocarbon atmosphere of arc discharge *Nanotechnology* **35** 385601
[15] Cheung C L, Kurtz A, Park H and Lieber C M 2002 Diameter-controlled synthesis of carbon nanotubes *J. Phys. Chem.* B **106** 2429–33
[16] Nasibulin A G, Pikhitsa P V, Jiang H and Kauppinen E I 2005 Correlation between catalyst particle and single-walled carbon nanotube diameters *Carbon* **43** 2251–7
[17] Zhang X, Graves B, De Volder M, Yang W, Johnson T, Wen B, Su W, Nishida R, Xie S and Boies A 2020 High-precision solid catalysts for investigation of carbon nanotube synthesis and structure *Sci. Adv.* **6** eabb6010
[18] Chen G, Seki Y, Kimura H, Sakurai S, Yumura M, Hata K and Futaba D N 2014 Diameter control of single-walled carbon nanotube forests from 1.3–3.0 nm by arc plasma deposition *Sci. Rep.* **4** 3804
[19] Kesälä E, Kuronen A and Nordlund K 2007 Molecular dynamics simulation of pressure dependence of cluster growth in inert gas condensation *Phys. Rev.* B **75** 174121
[20] Voloshko A, Colombier JP and Itina T E 2015 Comparison of laser ablation with spark discharge techniques used for nanoparticle production *Appl. Surf. Sci.* **336** 143–9
[21] Itina T E and Voloshko A 2013 Nanoparticle formation by laser ablation in air and by spark discharges at atmospheric pressure *Appl. Phys.* B **113** 473–8
[22] Quesnel E, Pauliac-Vaujour E and Muffato V 2010 Modeling metallic nanoparticle synthesis in a magnetron-based nanocluster source by gas condensation of a sputtered vapor *J. Appl. Phys.* **107** 054309

[23] Vishnyakov V I, Kozytskyi S V and Ennan A A 2019 Features of nucleation in welding fumes from gas metal arc welding *J. Aerosol. Sci.* **137** 105439

[24] Girshick S L and Chiu C 1990 Kinetic nucleation theory: a new expression for the rate of homogeneous nucleation from an ideal supersaturated vapor *J. Chem. Phys.* **93** 1273–7

[25] Khrabry A, Kaganovich I D, Nemchinsky V and Khodak A 2018 Investigation of the short argon arc with hot anode. I. Numerical simulations of non-equilibrium effects in the near-electrode regions *Phys. Plasmas* **25** 013521

[26] Yatom S, Khrabry A, Mitrani J, Khodak A, Kaganovich I, Vekselman V, Stratton B and Raitses Y 2018 Synthesis of nanoparticles in carbon arc: measurements and modeling *MRC* **8** 842–9

[27] Fang X, Shashurin A, Teel G and Keidar M 2016 Determining synthesis region of the single wall carbon nanotubes in arc plasma volume *Carbon* **107** 273–80

[28] Kundrapu M and Keidar M 2012 Numerical simulation of carbon arc discharge for nanoparticle synthesis *Phys. Plasmas* **19** 073510

[29] Hagena O F 1981 Nucleation and growth of clusters in expanding nozzle flows *Surf. Sci.* **106** 101–16

[30] Yamada I, Usui H and Takagi T 1987 Formation mechanism of large clusters from vaporized solid material *J. Phys. Chem.* **91** 2463–8

[31] Wegner K, Walker B, Tsantilis S and Pratsinis S E 2002 Design of metal nanoparticle synthesis by vapor flow condensation *Chem. Eng. Sci.* **57** 1753–62

[32] Panda S and Pratsinis S E 1995 Modeling the synthesis of aluminum particles by evaporation-condensation in an aerosol flow reactor *Nanostruct. Mater.* **5** 755–67

[33] Zhang L, Zhang L, Yu B, Wang R and Yang F 2023 Dynamic evolution of metal nanoclusters revealed by *in-situ* electron microscopy *J. Appl. Phys.* **56** 413001

[34] Zeldovich Y B 1992 *On the Theory of New Phase Formation: Cavitation* ed R A Sunyaev (Princeton University Press) pp 120–37

[35] Mcmurry P H and Friedlander S K 1978 Aerosol formation in reacting gases: relation of surface area to rate of gas-to-particle conversion *J. Colloid Interface Sci.* **64** 248–57

[36] Nemchinsky V A and Shigeta M 2012 Simple equations to describe aerosol growth *Model. Simul. Mat. Sci. Eng.* **20** 045017

[37] Keene B J 1988 Review of data for the surface tension of iron and its binary alloys *Int. Mater. Rev.* **33** 1–37

[38] Vapor pressure calculator [IAP/TU Wien] (available at: www2.iap.tuwien.ac.at/www/surface/vapor_pressure) (Accessed 1 September 2023

[39] Clementi E, Raimondi D L and Reinhardt W P 1967 Atomic screening constants from SCF functions. II. atoms with 37–86 electrons *J. Chem. Phys.* **47** 1300–7

[40] Feder J, Russell K C, Lothe J and Pound G M 1966 Homogeneous nucleation and growth of droplets in vapours *Adv. Phys.* **15** 111–78

[41] Tikkanen V, Reischl B, Vehkamäki H and Halonen R 2022 Nonisothermal nucleation in the gas phase is driven by cool subcritical clusters *Proc. Natl Acad. Sci.* **119** e2201955119

[42] Beutl M, Pottlacher G and Jäger H 1994 Thermophysical properties of liquid iron *Int. J. Thermophys.* **15** 1323–31

[43] Yang H, Song G and Hogan C J 2022 A molecular dynamics study of collisional heat transfer to nanoclusters in the gas phase *J. Aerosol. Sci.* **159** 105891

[44] Lenev D Y and Norman G E 2019 Molecular modeling of the thermal accommodation of argon atoms on clusters of iron atoms *High Temp.* **57** 490–7

[45] Sipkens T A and Daun K J 2018 Effect of surface interatomic potential on thermal accommodation coefficients derived from molecular dynamics *J. Phys. Chem.* C **122** 20431–43

[46] Daun K J, Sipkens T A, Titantah J T and Karttunen M 2013 Thermal accommodation coefficients for laser-induced incandescence sizing of metal nanoparticles in monatomic gases *Appl. Phys.* B **112** 409–20

[47] Kock B F, Kayan C, Knipping J, Orthner H R and Roth P 2005 Comparison of LII and TEM sizing during synthesis of iron particle chains *Proc. Combust. Inst.* **30** 1689–97

[48] Eremin A, Gurentsov E and Schulz C 2008 Influence of the bath gas on the condensation of supersaturated iron atom vapour at room temperature *J. Phys. D: Appl. Phys.* **41** 055203

[49] Gutsev G L and Bauschlicher C W 2003 Interaction of carbon atoms with Fen, Fen−, and Fen+ clusters (n=1–6) *Chem. Phys.* **291** 27–40

[50] Ding F, Bolton K and Rosén A 2004 Nucleation and growth of single-walled carbon nanotubes: a molecular dynamics study *J. Phys. Chem.* B **108** 17369–77

[51] Allouche A and Ferro Y 2006 Dissociative adsorption of small molecules at vacancies on the graphite (0001) surface *Carbon* **44** 3320–7

[52] T.p. B Jr, Goodman D W, Kay B D and Yates J T Jr 1987 Kinetics of the activated dissociative adsorption of methane on the low index planes of nickel single crystal surfaces *J. Chem. Phys.* **87** 2305–15

[53] Hong S 2003 Surface energy anisotropy of iron surfaces by carbon adsorption *Curr. Appl Phys.* **3** 457–60

[54] Lua A C and Wang H Y 2013 Decomposition of methane over unsupported porous nickel and alloy catalyst *Appl. Catal.* B **132–133** 469–78

[55] Schouten F C, Gijzeman O L J and Bootsma G A 1979 Interaction of methane with Ni(111) and Ni(100); diffusion of carbon into nickel through the (100) surface; An aes-leed study *Surf. Sci.* **87** 1–12

[56] Baker F S and Brink G O 1962 Adsorption of potassium beams on surfaces *J. Chem. Phys.* **37** 1012–7

[57] Desai P D 1986 Thermodynamic properties of iron and silicon *J. Phys. Chem. Ref. Data* **15** 967–83

[58] Boer J H 1968 *The Dynamical Character of Adsorption* (Clarendon P)

[59] Musikhin S, Raitses Y and Nemchinsky V, High-speed 2D 2-color pyrometry of electrodes in arc discharge (in preparation)

[60] Guéret C, Daroux M and Billaud F 1997 Methane pyrolysis: thermodynamics *Chem. Eng. Sci.* **52** 815–27

[61] Fincke J R, Anderson R P, Hyde T A and Detering B A 2002 Plasma pyrolysis of methane to hydrogen and carbon black *Ind. Eng. Chem. Res.* **41** 1425–35

[62] Friedlander S K 2000 *Smoke, Dust, and Haze: Fundamentals of Aerosol Dynamics* 2nd edition (Oxford University Press)

[63] Smirnov B M 2010 *Cluster Processes in Gases and Plasmas* (Wiley)

[64] Boulos M I, Fauchais P and Pfender E 2013 *Thermal Plasmas: Fundamentals and Applications* (Springer)

[65] Monaghan B J and Quested P N 2001 Thermal diffusivity of iron at high temperature in both the liquid and solid states *ISIJ Inter.* **41** 1524–8

[66] Tibbetts G G 1980 Diffusivity of carbon in iron and steels at high temperatures *J. Appl. Phys.* **51** 4813–6